PNAS Nexus, 2024, 3, pgae501
https://doi.org/10.1093/pnasnexus/pgae501
Advance access publication 10 December 2024
Research Report

How do roses build failure-resistant anchoring tools?

Liat Levavi [a] and Benny Bar-On [a,*]

[a]Department of Mechanical Engineering, Ben-Gurion University of the Negev, Beer Sheva 84105, Israel
*To whom correspondence should be addressed: Email: bbo@bgu.ac.il
Edited By Yannis Yortsos

Abstract

Rose prickles are small-scale, plant-based anchoring tools of multifunctional biomechanical roles, combining physical defense against herbivores and growth support on surrounding objects. By employing multiscale structural observations, nanomechanical characterizations, and finite-element simulations, we unveil that the dog rose (*Rosa canina* Linnaeus) prickle incorporates structural–mechanical modifications at different length scales, resulting in macroscopic stress-locking effects that provide the prickle extreme damage-resistant capabilities and secure its functional form against catastrophic failures. These functional design strategies, unique to plant-based biomechanical tools, may promote futuristic micro-engineered anchoring platforms for micro-robotics locomotion, biomedical microinjection, and micromechanical systems.

Keywords: plants biomechanics, multiscale structural mechanics, load-bearing, finite-element simulations, functional adaptation

Significance Statement

Rose shrubs possess miniature epidermal appendages (prickles) that provide them with crucial biomechanical capabilities (physical defense and growth support). The dog rose prickles (*Rosa Canina* Linnaeus) incorporate intimate relationships between their geometrical shape, microstructural density, and nanomechanical properties, making them multifunctional anchoring tools with outstanding resistance to mechanical failures. This unusual "design solution" of biomechanical tools in the plant kingdom may promote the development of innovative micro-anchoring platforms for diverse applications.

Introduction

Plants possess a variety of small-scaled, curve-shaped, and sharp-edged anchoring tools in the forms of spines, thorns, and prickle, providing them essential biomechanical functions, including physical defense against herbivores and frictional contact for growth support (1–4). Among these, rose prickles are specifically recognized by their hard and sharp tips that easily puncture and tear softer target objects alongside their overall high rigidity and damage resistance that preserve their shapes mostly undeformed and undamaged even upon significant mechanical loadings (5). While the botanical aspects of rose prickles, e.g. formation process, morphological characteristics, and anatomical composition, have been extensively studied over the years (6–10), their hierarchical structures and biomechanical load-bearing characteristics are still largely unexplored. Identifying the structural mechanics principles of rose prickles is a critical milestone toward understanding how plants evolve and adapt their anchoring tools to promote their herbivory defense and growth support functions; practically, these insights may open new horizons for advanced engineering developments of miniature, high-performance anchoring platforms for various applications (11, 12).

Rose prickles integrate distinct structural characteristics at different length scales. On the macroscopic level, their geometrical shapes exhibit pronounced widening from their sharp tip toward the underlying stem with different aspect ratios along the stem axis and at the stem circumference, which globally links to a universal geometrical law of various nonplant sharped-edge biomechanical tools of different sizes and shapes (e.g. stingers, fangs, and teeth) (13). On the material level, the prickles are fundamentally biological composites made of highly lignified cellular tissues (exterior epidermis and interior cortical) of spatially varying microstructural characteristics (i.e. sizes, shapes, and cell wall thicknesses) (5, 7). The composite characteristics of the prickles are specifically modified near their tip and close to their exterior surface—analogously to various anchoring tools in nonplant systems, such as arthropod claws, squid beaks, and worm jaws (14, 15)—which implies their mechanical adaptation in terms of functional load bearing. Indeed, extensive mechanical experiments on rose prickles shed light on their significant damage resistance, where overload failures never occurred within the bulk prickle but only at its connection site with the stem (5, 16). To the best of our knowledge, the origins of these damage-resistant

Competing Interest: The authors declare no competing interests.
Received: May 27, 2024. **Accepted:** October 25, 2024

characteristics have yet to be discovered, and more broadly, the fundamental load-bearing characteristics of the prickles and their relationships to their diverse biomechanical functions have yet to be explored.

The failure process of load-bearing plant organs is inherently complex due to their internal composite architectures and pronounced microstructural anisotropy. These characteristics give rise to various, nonclassical, toughening mechanics that detain, direct, and even prevent their fracture paths (17, 18). For example, basal failure of rose prickles is a priori unpredictable, which may occur within the directional tissue of the prickle itself, below the prickle, above or beneath the interfacial cork layer, or at nondirectional cortical parenchyma of the stem. Each failure type incorporates distinct fractured surfaces with different fracture paths and follows different force–displacement trends until complete failure (5, 7). Although a profound failure criterion is currently not in hand, the von Mises stress and the principle tensile stress may be considered as possible indicators for the onset of mechanical damage and a failure sequence within the prickle. The von Mises stress indicator corresponds to a distortion-driven failure, suitable for ductile engineering materials and conventionally employed, experimentally supported, in various biomechanical elements (19–23). The principal tensile stress indicator corresponds to a stretching failure, suitable for brittle engineering materials and, thus, for dry plant parts. Specifically, the local orientation of the principal stress represents a critical stretching-failure axis within the plant part, which is commonly resisted by the local microstructural anisotropy of the underlying tissues (24, 25).

In this study, we employ multiscale structural observations, nanomechanical experiments, and numerical simulations to disclose the fundamental structure–mechanics–function relationships of rose prickles, focusing on the prickles of the *Rosa canina* Linnaeus (dog rose) shrub as a model system of our analysis. To this end, we employ macroscale and microscale computed tomography (CT) and scanning electron microscopy (SEM) to characterize the hierarchical structure of the prickle across the millimeter-to-micrometer length scales and nanoindentation experiments to identify nanomechanical properties of its basic microstructural materials. Then, we integrate these findings into finite-element (FE) simulations on the native structural forms of the prickles, disclose their stress morphologies at puncturing, hanging, and anchoring functional states, and unveil how the geometrical and material characteristics of the prickle reciprocally evolved, and possibly adapted, to promote its biomechanical load bearing and to secure its form against catastrophic failure.

Materials and methods

Samples

Dry samples of *Rosa canina* L. branches, coated with prickles, were received from the "Wahl Rose Garden" in Jerusalem, Israel. The prickles were cut from the stem by a scalpel and stored at room temperature.

Computed tomography

CT scans of the prickles were conducted with SkyScan (Bruker, MA). For low-resolution CT scans of the whole prickle, a SkyScan-1072 scanner was used with the following parameters: voxel size 6–9 μm^3, voltage 40 kW, current 100 μA, and exposure time 3,000 ms. For high-resolution CT (μCT) scans of local regions within the prickle, a SkyScan-1272 scanner was used with the following parameters: voxel size 0.8 μm^3, voltage 40 kV, current 100 μA, and exposure time 2,000 ms. The images were reconstructed with NRecon 1.7.5.9 and DataViewer 1.6 software (Bruker). Volume fraction analyses, visualizations (artificially colored), and segmentation for the FE model were conducted with Avizo 9.3 software (Thermo Fisher Scientific, Germany).

Scanning electron microscopy

SEM observations were conducted with either (i) FEI Phenom XL G2 (Thermo Fisher Scientific) with secondary electron (SE) and backscatter electron detectors, 5–10 kV, or (ii) FEI Verios 460L (Thermo Fisher Scientific) at SE mode, using an Elstar in-lens and Everhart–Thornley detectors, 3 kV, 25 pA. Both free-fractured and embedded–polished samples were analyzed after a 15 nm gold coating.

Image analysis

Geometrical and cross-sectional image analysis was conducted by built-in algorithms in MATLAB 2021b. The geometrical shape and ventral edge characterizations were conducted by using Kirsch's compass masks algorithm on lateral images of the prickle. The cross-sectional analysis was conducted by using regionprops algorithm for edge detection and axes measurements of the oval cross-sections. Volume fraction analysis of the microtubular arrays within the different regions of the prickle was conducted by using ImageJ (v1.54f) and Fiji (ImageJ2) open-source software tools (imagej.net) on SEM and CT images.

Nanoindentation experiments

Indentation experiments were conducted with the Hysitron Tribоindenter-950 (Bruker) with a Berkovich tip. Prior to the experiments, samples were embedded in cold mounting epoxy and then cut-polished. The nanoindentation experiments were conducted on cross-sections of the samples following a load-control protocol: linear loading for 5 s and up to a maximal force of 70 μN, a constant maximal force for 2 s, and then linear unloading for 5 s. The nanoindentation analysis followed the Oliver–Pharr method and yielded the indentation modulus and indentation hardness (26).

Statistical analysis

Statistical tests for the measured indentation modulus, indentation hardness, and contact resistance were performed in MATLAB 2021b. Nonparametric Mann–Whitney U test or Kruskal–Wallis test was used for comparison between two or three groups, respectively, with Tukey's post hoc test. The statistical distributions of the measured parameters were extracted by a standard transformation of Weibull's coordinates, yielding Weibull's cumulative distribution function for each parameter, namely $CDF(X) = 1 - \exp[-(X/X_0)^{\kappa}]$, where X_0 and κ are the Weibull's scale and shape factors, respectively.

FE simulations

FE simulations were conducted with commercial software (ABAQUS/standard 6.14). The analysis was carried out on reconstructed geometrical models from the CT analysis segmented by four-node, 3D linear-elastic tetrahedral elements (C3D4, ABAQUS element library). The simulation models included overall ~10^4 elements with isotropic linear-elastic material models suitable for plant tissues (25, 27, 28). Each prickle region (uniform, skin, and core) was segmented separately, and the segmented regions were combined using full (nonslip) contact conditions. The Young's moduli of the different regions were set via Voigt's model as the typical measured indentation modulus of the cell walls

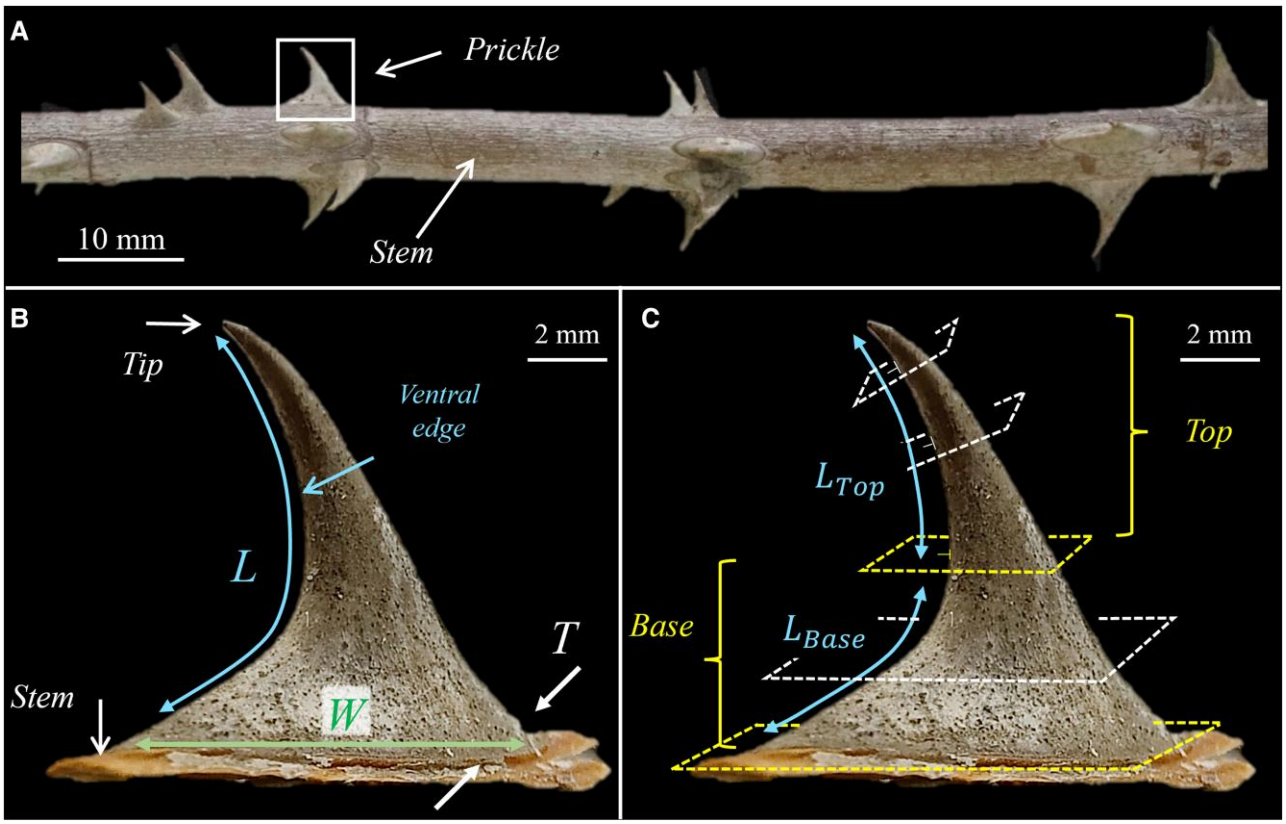

Fig. 1. Geometrical shape of the *Rosa canina* L. prickle. A) A stem with several prickles. B) A single prickle. *L* is the overall length of the ventral edge of the prickle from tip to base. *W* and *T* are the maximal width and thickness of the prickle at the connection site of the prickle and the stem. *W* spans along the stem axis, and *T* spans along stem circumference. C) The local normal cross-sections at the top part of the prickle are locally parallel to the ventral edge; the local normal cross-sections at the base part of the prickle are globally parallel to the surface of the stem. The ventral lengths of the top and base parts of the prickle are L_{Top} and L_{Base}, respectively. The structural parameters of the prickle are summarized in Table S1.

(10 *GPa*) multiplied by the typical measured microtubular density of each region (0.8 density for the uniform and skin regions and 0.5 density for the core region), and their Poisson's ratios are set as $\nu = 0.3$. The simulation models incorporated pressure loadings on the top part of the prickle that corresponded to the specific functional states analyzed with fixed-displacement boundary conditions on the bottom surface (i.e. stem connection site). The FE analysis yielded the stress morphology (σ; von Mises stress or principal stress) within the prickle, scaled by the magnitude of the pressure loading (p), as well as its maximal stress characteristics (location and magnitude).

Results

Hierarchical structure and material characteristics

Structural parts

The geometrical shape of the *R. canina* prickle resembles a sickle with a tapered structure that expands from the tip toward the stem (Fig. 1A–B). The total length of the ventral edge of the prickle is *L*; the maximal width (*W*) and thickness (*T*) of the prickle are at its connection site with the stem surface, where $W \sim L$ spans along the stem axis and $T \sim L/3$ spans the stem circumference, respectively (Table S1). The ventral edge of the prickle includes a single normal plane parallel to the stem surface—separating the prickle to distal top and proximal base parts relative to the stem (Fig. 1C). The ventral lengths of the top and base parts are approximately half of the overall ventral length of the prickle, i.e. $L_{Top} \sim L_{Base} \sim L/2$ (Table S1). The top and base parts of the prickle follow different cross-sectional orientations due to a curvature change of the dorsal edge from convex (top part) to concave (base part). Cross-sections at the top part are locally parallel to the ventral edge, whereas cross-sections at the base part are globally parallel to the surface of the stem (Fig. 1C).

The cross-sections of the prickle are oval shaped of local width $w(x)$ and local thickness $t(x)$, where $0 \le x \le L$ indicates the location along the ventral edge from the tip ($x = 0$) to the stem ($x = L$) (Fig. 2A, Movie S1). Close to the tip, the cross-sections are pseudo-circular, and the datasets of $w(x)$ and $t(x)$ highly overlap and mildly change (Fig. 2B). After a certain distance from the tip, the cross-sections transform into pseudo-elliptical, and the datasets of $w(x)$ and $t(x)$ branch from one another, become statistically different, and eventually separate. The pseudo-elliptical cross-sections further expand and significantly flatten along the base part of the prickle, where $w(x)$ and $t(x)$ follow linear trends of different slopes and reach their maximal values at the stem, i.e. $w(x = L) = W$ and $t(x = L) = T$ (Fig. 2C).

Accordingly, the overall shape of the prickle incorporates two distinct structural parts: (i) an initial sharpened needle-like part that is located close to the tip (ventral length $L_{Needle} \sim L/4$) and (ii) a massive, flattened blade-like part that is located afterward and ends at the stem (ventral length $L_{Blade} \sim 3L/4$) (Fig. 2D).

Material characteristics

The prickle incorporates distinct regions of higher-density (HD) and lower-density (LD) materials, represented by the bright and

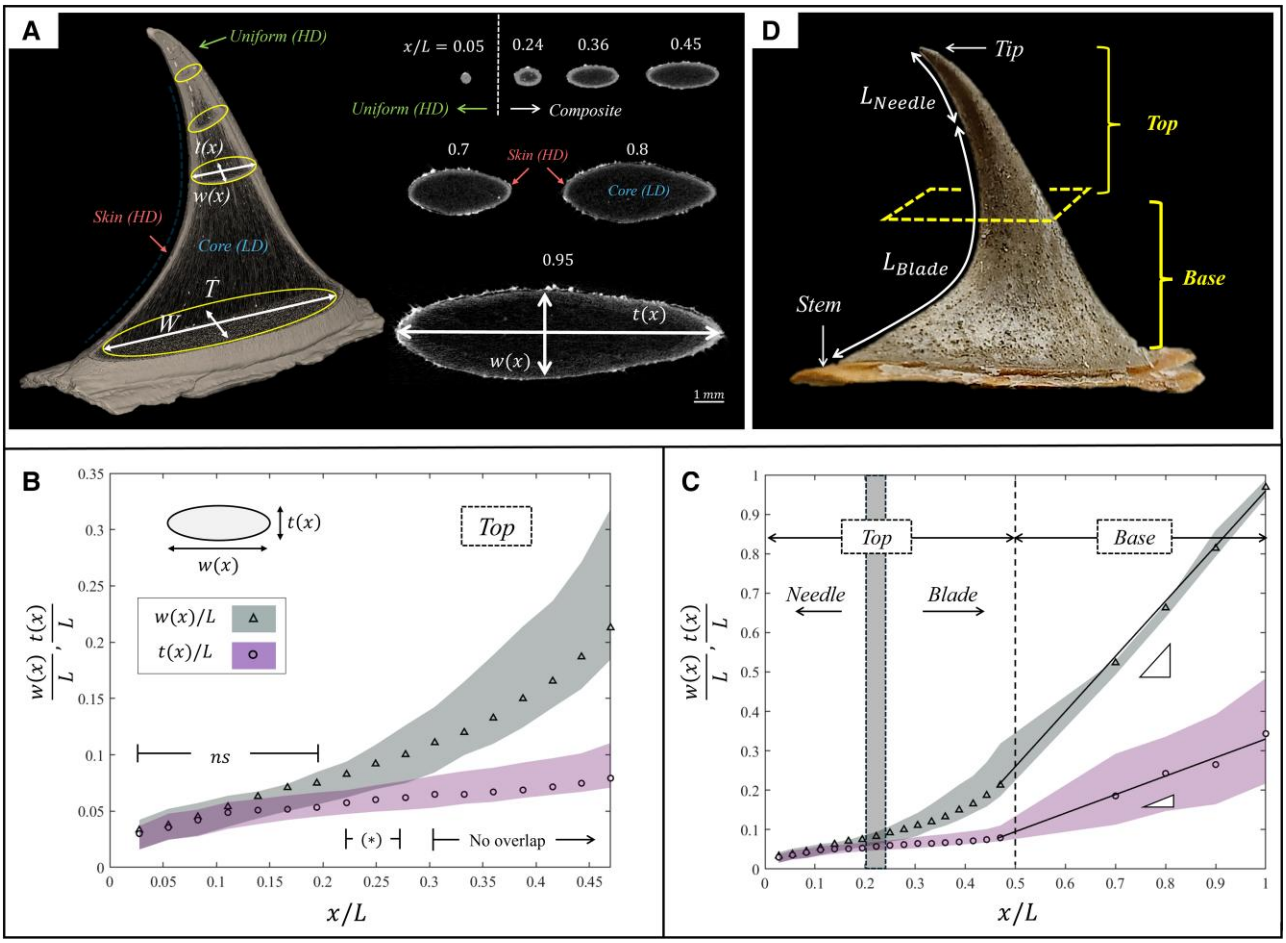

Fig. 2. Cross-sectional geometry of the *Rosa canina* L. prickle. A) µCT image of the prickle with *x* indicating the location along the ventral edge (left) and selected cross-sectional images of the prickle in different locations (right). The cross-sectional shape is oval, with width *w*(x) and thicknesst(x), respectively. Bright regions indicate a high-density material, and the dark regions indicate a low-density material. B) Variations in *w*(x) and *t*(x) along the top part of the prickle. Shaded areas indicate the range of the datasets, and symbols indicate their medians ($n = 5$). (*) indicates significant statistical differences between the *w*(x) and *t*(x) datasets ($P < 0.05$; Wilcoxon's rank sum test). C) Variations in *w*(x) and *t*(x) along the entire ventral edge of the prickle. The median values of *w*(x) and *t*(x) follow liner trends throughout the base part of the prickle, i.e. $w(x) \propto \alpha_w \cdot (x)$ and $t(x) \propto \alpha_t \cdot (x)$, where $\alpha_w = 1.41$ ($R^2 = 0.99$) and $\alpha_t = 0.68$ ($R^2 = 0.98$). D) The structure of the prickle comprises an initial needle-like region of ventral length L_{Needle} followed by a blade-like region of ventral length L_{Blade} (gray shaded rectangle indicates the variability range) (Table S1).

dark areas of the CT imaging (Fig. 2A). Cross-sections close to the tip include a uniform (HD) material (ventral length L_{Uni}), and cross-sections that are more distant from the tip are composites of peripheral skin (HD) that encloses a central core (LD) (ventral length L_{Comp}) (Fig. 3A, Table S1). The thickness of the skin is small (~0.03*L*) and mildly changes throughout the prickle, whereas the core gradually expands with the cross-sectional area toward the stem. Notably, the relative ventral lengths of the needle-like part and of the uniform material region, L_{Needle}/L and L_{Uni}/L, are highly overlapping—suggesting that the distinct structural parts and distinct material regions of the prickle are, in fact, tightly linked to one another, i.e. uniform needle and composite blade.

All material regions of the prickle are internally architected as microtubular arrays of a few micrometer-thick cell walls that enclose hollow interiors (Fig. 3B–D). At the top part of the prickle, these microtubular arrays are locally parallel to the ventral edge (i.e. normal to the cross-section). At the base part of the prickle, the microtubular arrays within the core region are globally normal to the surface of the stem (i.e. normal to the cross-section), whereas the microtubular arrays within the skin region are locally parallel to the exterior surface of the prickle (Fig. 3A, E–G). µCT-based and SEM-based volumetric analysis of the cell walls indicated high microtubular density within uniform and skin regions (~80%) and low microtubular density within the core region (~50%) (Table S2). Notably, the microtubular density is locally extreme at the apex of the prickle (~95%), i.e. close to that of a bulk solid.

Nanomechanical characteristics

Nanoindentation measurements on the cell walls yielded the indentation modulus (*E*) and hardness (*H*) of the microtubular arrays at the different material regions within the prickle (Fig. 4, Table S2). The results for both *E* and *H* are significantly different between the uniform, skin, and core regions, and their statistical CDFs tightly follow Weibull's form. The uniform region exhibits the highest hardness (*H*), the skin region exhibits the highest modulus (*E*), and the core region exhibits the lowest nanomechanical characteristics (both *H* and *E*). The ratio H^3/E^2 of the paired $E - H$ nanoindentation data indicates a resistance to contact damage (i.e. the onset of contact plasticity (29)); this characteristic is relevant here for the uniform and skin regions of the

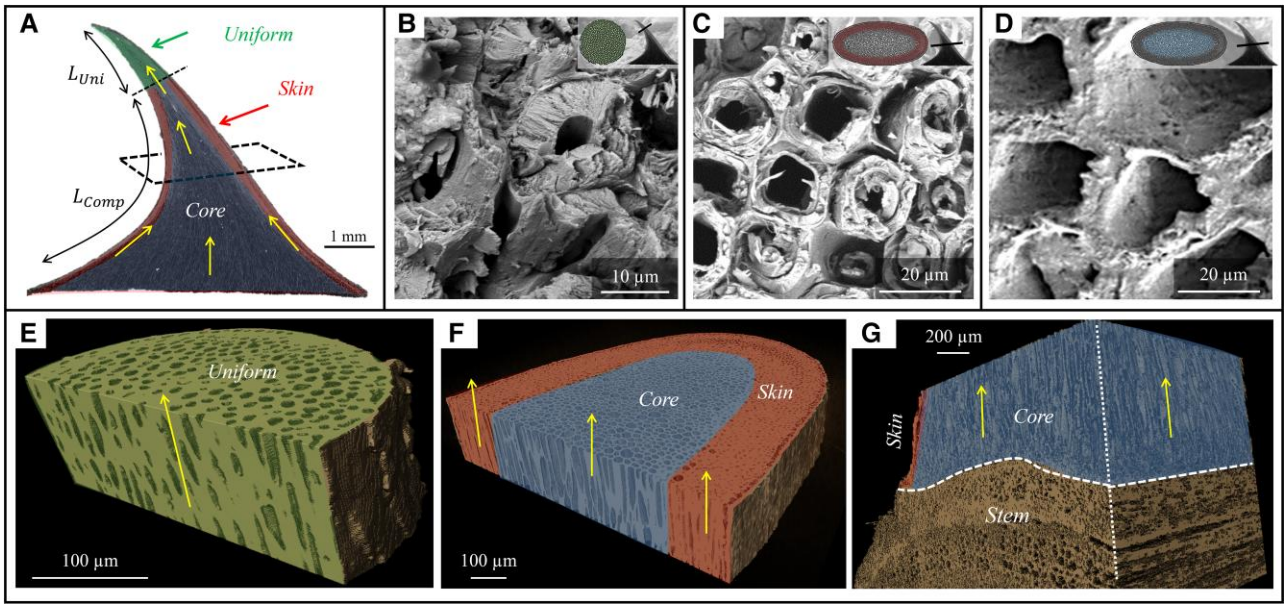

Fig. 3. Cross-sectional material of the *Rosa canina* L. prickle. A) µCT image of the prickle. The green shaded region indicates the uniform region close to the tip; the red shaded region and blue shaded regions indicate the skin and core regions of the prickle. L_{Uni} and L_{Comp} indicate, respectively, the ventral lengths of the uniform and the composite cross-sectional regions of the prickle (Table S1). Yellow arrows schematically indicate the local orientations of the microtubular arrays within the prickle. SEM images of the microtubular arrays within the uniform (B), skin (C), and core (D) regions of the prickle. Cross-sectional µCT images of the microtubular arrays at the uniform (E) and composite (F) cross-sectional regions of the prickle. Yellow arrows indicate the local orientation of the microtubular arrays. G) Frontal–sagittal µCT image of the prickle close to the stem. Yellow arrows indicate the local orientation of the microtubular arrays at the core, oriented perpendicular to the surface of the stem.

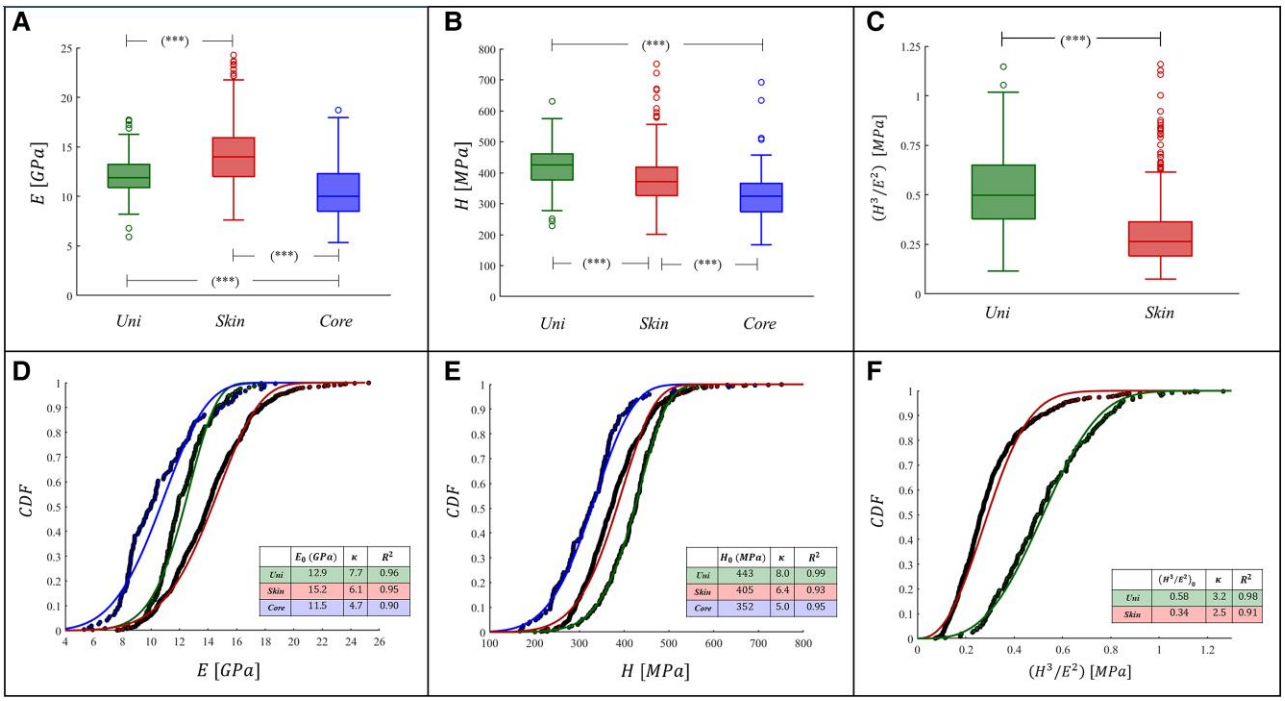

Fig. 4. Nanoindentation results for the cell walls of the prickle. A–C) Bar plots for the indentation modulus (E), indentation hardness (H), and contact-damage resistance (H^3/E^2) of the cell walls within the different material regions of the prickle. The upper and lower edges indicate the upper and lower quartiles, and the horizontal lines indicate the medians. The whiskers indicate the dataset range, and the circles indicate the outliers. D–F) Statistical representations of the datasets in (A–C) via Weibull's CDF. E_0, H_0, and $[H^3/E^2]_0$ are the corresponding Weibull's scale parameter, κ are their corresponding shape parameters, and R^2 are the coefficient of determination to Weibull's coordinates of each dataset.

prickle, which directly sustain the biomechanical loadings. The H^3/E^2 values of the uniform region are significantly higher than those of the skin region (Fig. 4C and F). Accordingly, the contact resistance of the needle-like part of the prickle is about twice that of the blade-like part.

A summary of the hierarchical structure and material characteristics of the *R. canina* prickle is shown in Fig. 5. These results are integrated next into FE simulations to analyze the biomechanical load-bearing characteristics at different functional states.

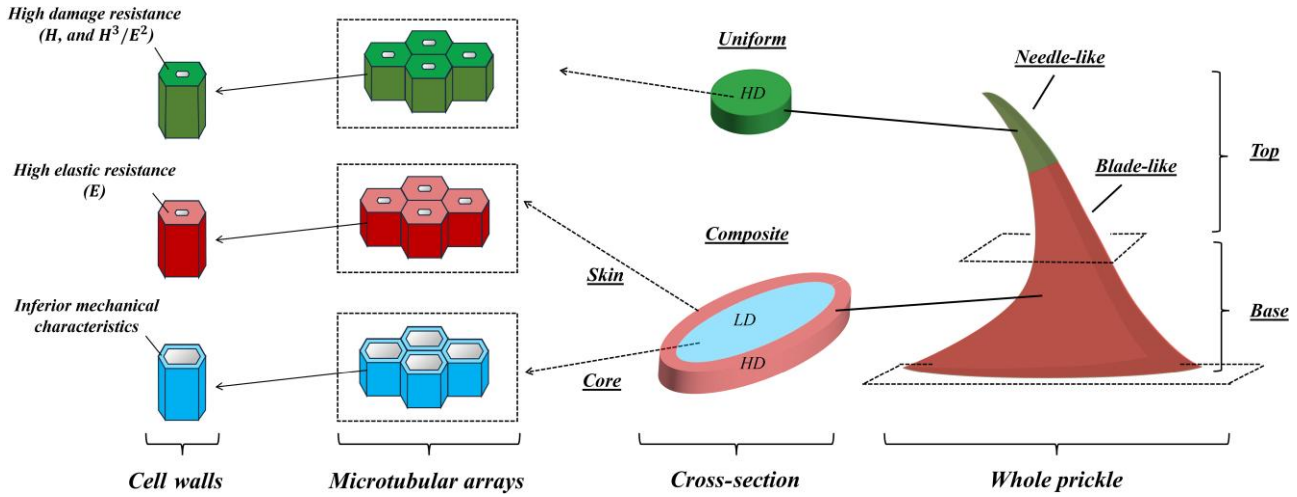

Fig. 5. Schematic illustration for the hierarchical structure of the *R. canina* prickle. The uppermost needle-like structure of the prickle includes a uniform, high-density microtubular material of high abrasion resistance. The subsequent blade-like structure of the prickle is a skin–core composite. The skin comprises a high-density microtubular material of high elastic resistance, and the core is a low-density microtubular material with inferior mechanical properties.

Biomechanical load bearing

The biomechanical load-bearing analysis of the prickle was carried out via FE simulations, focusing on its typical functional states: (i) puncturing of the prickle into target mediums (herbivory defense function) (Fig. 6A), (ii) local hanging of the prickle on surrounding objects (growth support function) (Fig. 6B), and (iii) anchoring of the prickle on rough surfaces or tearing through target mediums (growth support and herbivory defense functions, respectively) (Fig. 6C).

Puncturing

In the puncturing state, the apex of the prickle incorporated a directed pressure (i.e. traction) at different orientations (θ) within the sagittal plane—spanning between locally parallel ventral edge at the tip ($\theta = 0°$; target penetrating) to locally perpendicular to the ventral edge ($\theta = 90°$; target scratching) (Figs. 6A and 7). The FE simulations yielded the von Mises stress and the principal tensile stress morphologies within the prickle and indicated their local maximal values. The von Mises stresses of the prickle (Fig. 7A–B) reach maximal values at the near-tip region (σ_{max}) for all orientations, followed by a bending-like stress morphology throughout the top part of the prickle with high stresses on the ventral and dorsal edges of the prickle. The stress levels gradually decrease with the distance from the apex and become minor at the base part of the prickle. The orientation of the loading significantly affects the overall magnitude of the von Mises stress morphology and, specifically, of the maximal stress. The stresses are the smallest for loadings that are close to a penetration state ($\theta \approx 0°$), and they progressively increase with θ while exhibiting high sensitivity to its variations for combined penetration–scratching states ($\theta \approx 20°$–$60°$). Afterward, the stresses moderately increase with θ and exhibit mild sensitivity to its variations, and finally, they reach the highest values for loadings that are close to the scratching state ($\theta \approx 90°$). The principal tensile stresses (Fig. 7C–D) reach maximal values on the ventral edges of the prickle, which gradually increase with the loading direction from penetration to scratching, similar to the von Mises stress. For loadings that are close to a penetration state ($\theta \approx 0°$), the maximal tensile stress is much smaller than the von Mises stress and is located distant from the tip. For loadings that involve considerable scratching ($\theta \approx 60°$–$90°$), the maximal tensile stresses are practically comparable to the von Mises stresses and are located close to the tip.

Hanging

In the hanging state, the ventral edge of the prickle incorporated local normal pressure at different positions along the top part of the prickle (x/L_{top})—resulting in contact-like stresses underneath the loading with a local maximum (σ_{max}) that promotes local damage to the underlying material (Figs. 6B and 8). These contact-like stresses arise within the uniform material when the loading is applied closer to the tip and within the exterior skin when the loading is applied on the composite region of the prickle. The magnitude of σ_{max} is the highest for near-tip loadings, gradually decreases with the loading distance from the tip over a certain region, and remains approximately constant afterward. The trend change between increasing-to-constant σ_{max} corresponds to the transition between the uniform and the composite regions of the prickle (Table S1). Significantly, the two-fold difference between the extreme σ_{max} for near-tip loadings vs. the constant σ_{max} for distant loadings corresponds well to the contact resistance (i.e. H^3/E^2) of the underlying microtubular regions (Fig. 8).

Anchoring–tearing

In the anchoring–tearing state, the ventral edge of the prickle incorporated normal pressure loading spanning from the tip over a certain ventral length along the top part of the prickle (l/L_{Top}). As the loading length increases, the overall force (F) on the prickle increases—resulting in greater stress levels within the prickle that span over greater portions of its top and base parts (Fig. 6C). The von Mises stresses (Fig. 9B) and the principal stresses (Fig. S1) exhibit very similar characteristics that correspond to the classical beam theory. For short-range loadings that apply only on the needle-like part of the prickle (i.e. $l/L_{Top} < 1/2$), the maximal stress (σ_{max}) arises on the ventral edge close to the end of the loaded region (x_{max}), and both σ_{max} and x_{max} increase with the length of loading (l/L_{Top}). Significantly, σ_{max} and x_{max} exhibit trend changes when the loading exceeds the needle-to-blade connection site (i.e.

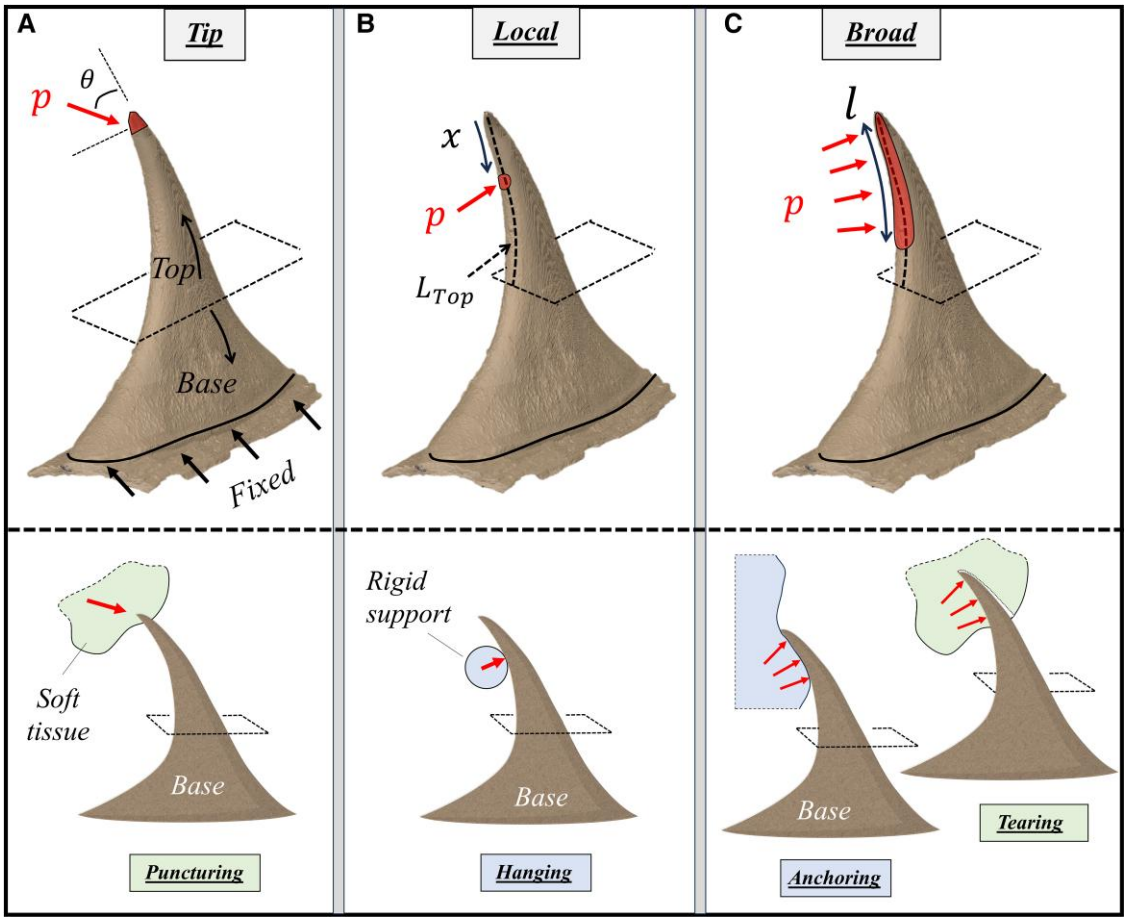

Fig. 6. Models for the biomechanical analysis of the *R. canina* prickle. A) Tip loading represents the puncturing of the prickle into target mediums (herbivory defense); B) local ventral loadings represent the leaning of the prickle on surrounding objects (growth support); C) broad ventral loadings represent tearing of the prickle throughout target mediums (herbivory defense) or anchoring of the prickle on rough surfaces (growth support). In (A), a directed pressure p (i.e. traction) is applied on the apex of the prickle at different orientations (θ) within the sagittal plane of the prickle. In (B), a local normal pressure p is applied at different ventral locations (x) along the top part of the prickle (length L_{Top}). In (C), a broad normal pressure p is applied on increasing ventral segments (length l), which span from the tip toward the base.

$l/L_{Top} \sim 1/2$), beyond which the magnitude and location of the maximal stress become approximately constant—even for long-range loadings that apply over significant portions of the blade-like part (Fig. 9C–D). This maximal stress-locking effect originates from the rapid increase in the cross-sectional moment of inertia due to the geometrical expansion of the blade-like part, preventing the emergence of significant bending stresses below the needle-to-blade connection site. Significantly, the FE results for local orientations of the principal stresses within the uniform, skin, and core regions of the prickle (Fig. 9E) correspond well to the actual microtubular orientations within the prickle (Fig. 3A).

Base widening

The base part of the prickle serves as a bridging region that gradually reduces the stresses within the prickle toward its mechanically weakened connection site with the stem (Figs. 9 and 10). The stress reduction effect is especially pronounced for long-range loadings, which yield broad stress morphologies throughout the majority of the prickle. To demonstrate the stress reduction effect, we modified the FE model with full-length pressure loadings by artificially excluding portions of the base part and observed the stress variations at the bottom surface of the model that correspond to the modified prickle–stem connection site. In the absence of the base part, the top part of the prickle directly connects to the stem, forming a sharp geometrical transition, of approximately right angle, between the ventral edge of the prickle and the long axis of the stem (Fig. 10A). This sharp geometrical transition yields stress intensification effects that produce extreme stress values at the prickle–stem connection site, which offends the load-bearing efficiency of the prickle and promotes its overloading catastrophic failure (i.e. complete traction). Notably, sharp transitions in cross-section cause stress concentrations is a central result of classical elasticity. The stresses at the connection site rapidly decrease, by a power low, while including larger portions of the base part (Fig. 10B–C)—both by blunting the prickle–stem geometrical transition and by expanding the total area of the connection site that decrease its effective force-to-area ratio. Notably, the connection stresses diminish by three orders of magnitude and become practically insignificant for the native prickle (i.e. with the whole base part) (Fig. 10D)—securing its weakened connection site with the stem against mechanical failure.

Discussion

The rose prickles belong to a large group of functional epidermal appendages located on the stems of various shrubs and even on the trunks of some tree species. Despite their miniature sizes and minor mass portions, rose prickles provide the shrub significant functional capabilities—by forming mechanical growth

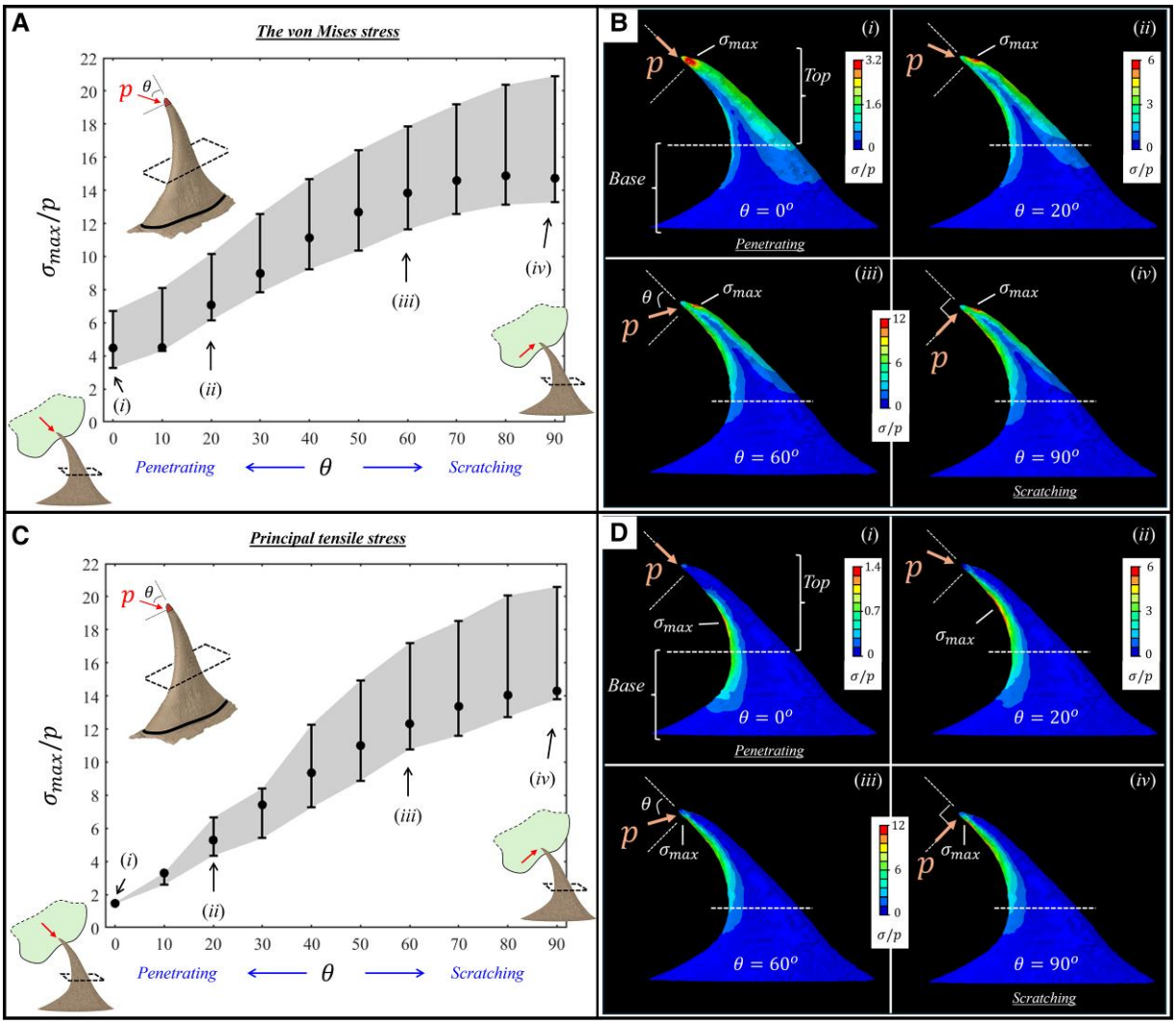

Fig. 7. FE results for the stresses (σ) of the prickle upon apex loadings (puncturing herbivory defense), showing the von Mises stresses (A–B) and the principal tensile stresses (C–D). A, C) Variations in the maximal stress (σ_{max}) within the prickle with the orientation of the tip loading (θ). The whiskers indicate the data range, and the symbols indicate the median values. B, D) Stress morphologies within the prickle for selected tip-loading orientations ($\theta = 0°$, 20°, 60°, and 90°). Specifically, $\theta = 0°$ corresponds to a penetration state with tip loading parallel to the ventral surface at the tip, and $\theta = 90°$ corresponds to a scratching state with tip loading perpendicular to the ventral surface at the tip. The results are scaled by the applied pressure (p).

support for its flexible stems via hanging on neighboring plants or anchoring into rough surrounding objects (e.g. rocks) and by deterring herbivores via puncturing, scratching, and tearing their mouthpart tissues. The multiple functions of the rose prickle intimately link to the overall load-bearing characteristics of its hierarchical structure—originated from the nanomechanical characteristics of its cell walls, upscaled through density-induced modifications of its microtubular arrays at different regions of the prickle, and finalized by graded geometrical characteristics of its macroscopic shape.

Failure resistance strategies of rose prickles

The rose prickle incorporates various structural–mechanical strategies to promote its failure resistance against diverse functional–mechanical loading states. In the puncturing state, the minimal stress for loadings close-to-parallel to the tip direction indicates that the prickle is primarily adapted to sustain penetration-dominant loadings, and its load-to-failure capabilities at this state are about two to three times greater than at the combined penetration–scratching and the scratching-dominant states. Moreover, the persistent near-tip location of the maximal stress for all loading states corresponds well to the extreme microtubular density at this region, providing the prickle with enhanced damage resistance to puncturing loadings. In the hanging state, the apparent correlation between the variations in the maximal stress and the contact resistance of the underlying material indicates a preannounced load-bearing adaptation that facilitates the hanging function of the prickle at different ventral positions. In the anchoring–tearing state, the maximal stress-locking effect promotes the load-bearing efficiency of the prickle by allowing it to magnify, and even double, the anchoring–tearing forces on target objects without increasing the maximal stress. Complementarily, the locking effect of the location of the maximal stress secures the prickle against catastrophic failures by confining its potential damage to the needle–blade connection site—preventing its further propagation within the blade-like part or downward to the prickle–stem connection site (i.e. blade fracture or prickle traction, respectively). The correspondence between the local orientations of the principal stresses

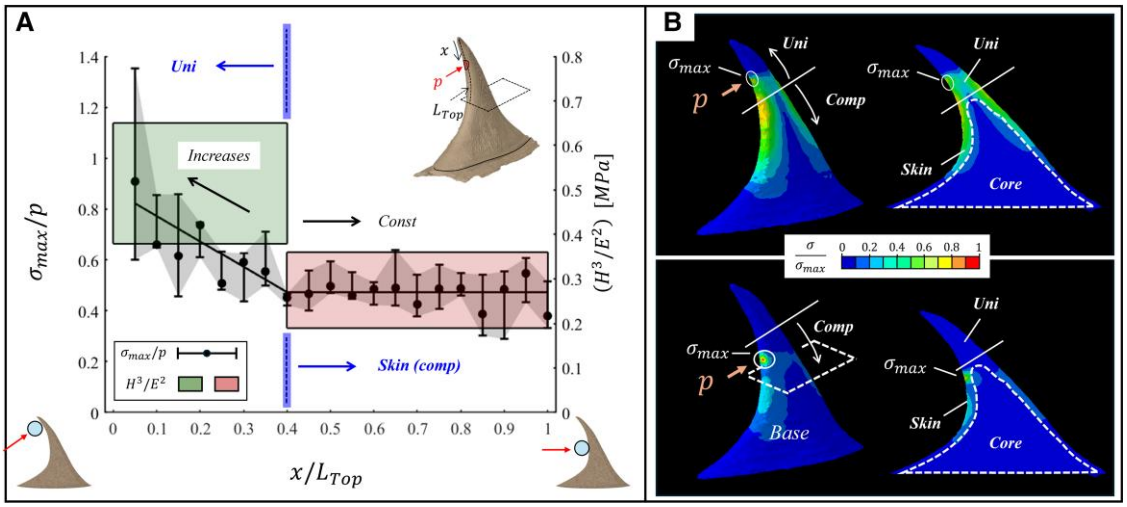

Fig. 8. FE results for the stresses ($\boldsymbol{\sigma}$, von Mises) of the prickle upon local ventral loadings (hanging growth support). A) Variations in the maximal stress (σ_{max}) underlying the pressure region with the relative loading location along the top part of the prickle (x/L_{Top}). The results are scaled by the applied pressure (p; left vertical axis). The whiskers indicate the data range, and the symbols indicate the median values. The green and red shaded regions refer to the interquartile range of the resistance to contact damage (H^3/E^2; right vertical axis) of the uniform and skin regions of the prickle, respectively. B) Representative stress morphologies within the prickle for local ventral loadings on the uniform region closer to the tip (top) and on the composite region closer to the base (bottom). Left panels: exterior stress morphologies of the prickle. Right panels: interior stress morphologies within the sagittal plane of the prickle; the uniform, skin, and core materials are indicated. The results are scaled by the maximal stress in each loading state.

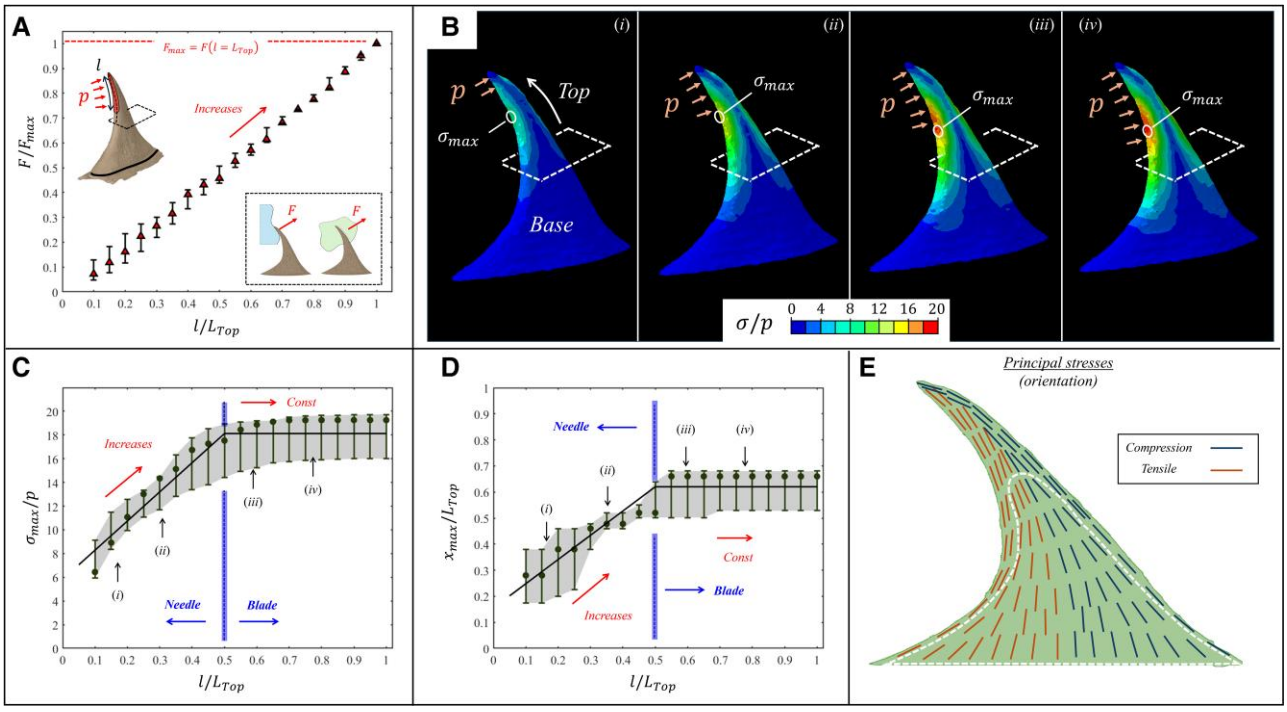

Fig. 9. FE results for the stresses ($\boldsymbol{\sigma}$) of the prickle upon broad ventral loadings (anchoring growth support or tearing herbivory defense). A) Variations in the overall force on the prickle (F) for increasing the ventral length of the pressure (l/L_{Top}), scaled by the maximal force for full-length pressure loading, $F_{max} = F(l/L_{Top} = 1)$. B) von Mises stress morphologies within the prickle for selected pressure lengths; (i) $l/L_{Top} = 0.15$, (ii) $l/L_{Top} = 0.35$, (iii) $l/L_{Top} = 0.6$, and (iv) $l/L_{Top} = 0.8$. The results are scaled by the applied pressure (p). The corresponding σ_{max} and x_{max} values for these cases are indicated in panels (C–D). C) Variations in the maximal stress within the prickle (σ_{max}) while increasing the ventral length of the applied pressure (l/L_{Top}). The results are scaled by the applied pressure (p). D) Variations in the location of the maximal stress (x_{max}) while increasing the length of the applied pressure (l/L_{Top}). The blue arrows indicate the ventral locations of the needle-like and the blade-like regions of the prickle. E) FE results for the local orientation of the dominating principal stresses (red—tension or blue—compression) within the sagittal plane of the prickle of the prickle; the white dashed line encloses the core region. The magnitudes of these principal stresses are shown in Fig. S1.

and the material anisotropy by the microtubular orientations gives rise to toughening mechanisms that resist mechanical failure within the bulk prickle, which is in line with previous experimental observations that failure typically occurs at the basal region below the prickle—either in the vicinity of the cork layer or within the stem tissue. Such basal failure is further

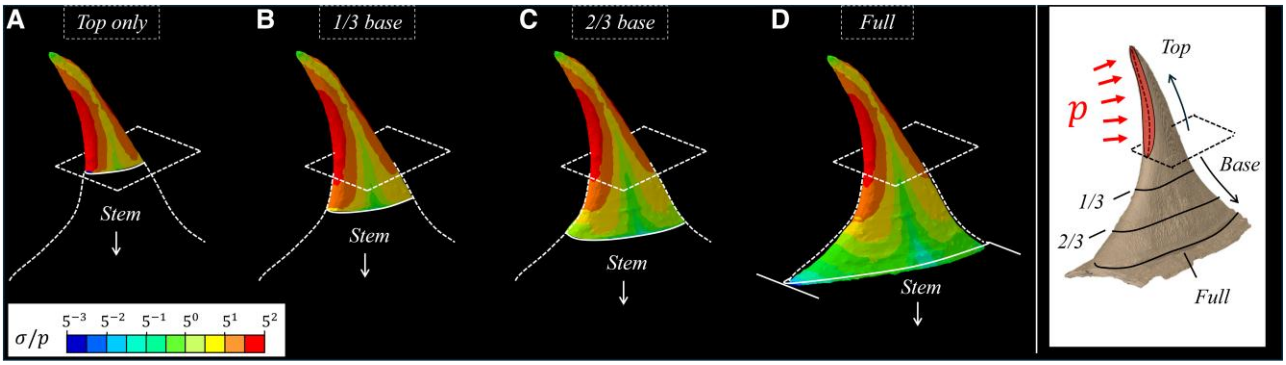

Fig. 10. FE results for the stresses (σ, von Mises) of the prickle upon broad ventral loadings with different base portions. A) Top part only; B–C) top part with 1/3 and 2/3 base portions; and D) top part with the entire base part. The results are presented on a logarithmic scale.

detained by the gradual base widening of the prickle, which prevents the emergence of stress concentrations due to sharp geometrical transitions between the prickle and the stem.

Links between rose prickles and other load-bearing biomechanical elements

The basic nanomechanical characteristics (E and H) of the cell walls comprising the rose prickle correspond well to those of plant tissues of pronounced mechanical roles (secondary xylem, sclerenchyma, and collenchyma), present in diverse types of load-bearing plant parts, including various of woods (30–33), nutshells (34), leaves (35), and winged seeds (36). The nanomechanical contact resistance (H^3/E^2) of the rose prickle is equivalent to nonplant biological materials that are functionally adapted to sustain contact loadings, including crab claws, squid beaks, spider claws, and fangs (37)—and, quite strikingly, exceeds that of most engineering steels and alloys (38). To the best of our knowledge, the contact resistance characteristic is firstly framed here in the context of plant biomechanics and, presumably, plays a significant role in other plant parts that sustain direct-contact loadings—both related to defense and growth functions (e.g. branch thorns, leaf spines, and fruit hooks) (39–41) and to shielding functions (fruit walls and seed shells) (34, 42, 43).

The high-density uniform and skin regions of the prickle effectively upscale the nanomechanical characteristics of their microtubular arrays into the material level—forming mechanically enhanced functional regions. The uniform region equips the prickle with a hard and contact-resistant tip that facilitates its puncturing capabilities into target mediums by generating stress concentrations and micro-damage effects that reduce their overall work-to-puncture (44–48). The exterior skin region equips the prickle with a stiff and hard coating that sustains its direct and indirect mechanical loadings, transmits their resultant stresses toward the stem, and promotes the overall structural resistance of the prickle to flexural deformations (49). Notably, the density-induced modifications of the rose prickle are analogous to chemical-induced and compositional-induced modifications found in various other nonplant biomechanical elements, e.g. metal-ion deposition that modifies the cutting edges of arthropod cuticular tools and marine worm jaws, and chitin content and alignment modification that reinforces the exocuticle parts of spider fangs and claws, and scorpion pincers (50–55).

The gradual morphological changes in the geometrical shape of the prickle form three distinct structural parts that fulfill different mechanical functions. The uppermost, puncturing, needle-like part of the prickle includes a semi-circular, slightly expanding cross-sectional shape that facilitates its puncturing efficiency by decreasing frictional loss (48, 56), enhancing its buckling stability (57, 58), and confining its puncturing stress-to-failure to the apex region (22, 59). Contrary to injection-related biomechanical elements that typically preserve their expanding semi-circular shapes throughout most of their structures (e.g. stingers, fangs, and spines (49, 58, 60–62)), the rose prickle breaks its axisymmetric expansion after a certain distance from the tip—modifying its remaining underlying into a flattened blade-like part that corresponds to miniature anchoring tools (e.g. insect claws, ant mandibles, and radular teeth (55, 63–65)). The oval cross-sectional expansion of the blade-like part facilitates the flexural rigidity of the prickle parallel to the stem axis, eliminates the evolution of significant bending stresses far from the tip, and confines the extreme stress states within the prickle to its near-tip region, which does not exceed the needle–blade connection site (49, 59). The final geometrical modification arises at the base part of the prickle, in which all cross-sections lay parallel to the stem axis, and their oval shapes exhibit pronounced aspect ratios that rapidly expand toward the connection site of the prickle with the stem. While such basal modification is typically absent in nonplant biomechanical elements (or very minimal, e.g. in some snake fangs (22, 62)), its presence is very dominant in rose prickles and apparently in various other plant anchoring elements (e.g. spines, thorns, trichomes, and fruit hooks) (5, 39, 40, 66). Evidently, the base part plays a significant role in protecting the weakened connection site of the prickle with the stem, thus securing the prickle against catastrophic traction failure.

Macroscopically, the stress morphologies within the prickle and the local orientation of the principal stresses closely follow the classical beam theory. This observation allows approaching the mechanical behavior of rose prickles and other sharp-edge biomechanical tools via analytical modeling tools of structural composites (67). Such models would possibly provide new insights into stress-to-failure characteristics of diverse forms of biomechanical tools and disclose other load-bearing aspects, such as graded deformation patterns, optimal structural stiffness, and puncture mechanics (68, 69), which may play critical roles in their functional capabilities.

Conclusions

The natural design principles of the rose prickle as a natural, plant-form anchoring tool demonstrate complementary structural and material adaptations that promote its load-bearing capabilities for multiple biomechanical functions. These design principles may open new horizons for developing advanced

engineering forms for miniature anchoring platforms for diverse applications (70–73).

Acknowledgments

The authors acknowledge the generous support of the Pearlstone Center for Aeronautical Engineering Studies, the scientific support from the Ilse Katz Institute for Nanoscale Science and Technology, and the valuable support of the Wahl Rose Garden (Jerusalem, Israel).

Supplementary Material

Supplementary material is available at *PNAS Nexus* online.

Funding

The authors declare no funding.

Author Contributions

L.L. carried out the structural observations, nanomechanical measurements, and FE simulations. B.B.-O. designed the research, and carried out the structural and mechanical modeling. All authors analyzed the data, discussed the results, and wrote the manuscript.

Data Availability

All data are available in the main text or the supplementary materials.

References

1 Hanley ME, Lamont BB, Fairbanks MM, Rafferty CM. 2007. Plant structural traits and their role in anti-herbivore. *Perspect Plant Ecol Evol Syst*. 8(4):157–178.
2 Rowe N, Isnard S. 2009. Biomechanics of climbing palms and how they climb. *Plant Signal Behav*. 4(9):875–877.
3 Halpern M, Waissler A, Dror A, Lev-Yadun S. 2011. Biological warfare of the spiny plant: introducing pathogenic microorganisms into herbivore's tissues. *Advances in applied microbiology (vol. 74)*. Academic Press. p. 97–116
4 Burris JN, Lenaghan SC, Stewart CN. 2018. Climbing plants: attachment adaptations and bioinspired innovations. *Plant Cell Rep*. 37(4):565–574.
5 Gallenmüller F, Feus A, Fiedler K, Speck T. 2015. Rose prickles and *Asparagus* spines–different hook structures as attachment devices in climbing plants. *PLoS One*. 10(12):e0143850.
6 Asano G, Kubo R, Tanimoto S. 2008. Growth, structure and lignin localization in rose prickle. *Bull Fac Agric*. 93:117–125.
7 Kellogg AA, Branaman TJ, Jones NM, Little CZ, Swanson JD. 2011. Morphological studies of Rubus prickles suggest that they are modified trichomes. *Botany*. 89(4):217–226.
8 Zhou N, Simonneau F, Thouroude T, Oyant LHS, Foucher F. 2021. Morphological studies of rose prickles provide new insights. *Hortic Res*. 8:221.
9 Amikura K, Ito H, Kitazawa MS. 2021. Discovery of spatial pattern of prickles on stem of Rosa hybrida 'Red Queen' and mathematical model of the pattern. *Sci Rep*. 11(1):13857.
10 Zhang Y, *et al.* 2024. Morphology, structure and development of glandular prickles in the genus Rosa. *Sci Hortic*. 326:112763.
11 Liu H, Liu S, Jiao J, Lu TJ, Xu F. 2017. Trichomes as a natural biophysical barrier for plants and their bioinspired applications. *Soft Matter*. 13(30):5096–5106.
12 Jeffries L, Lentink D. 2020. Design principles and function of mechanical fasteners in nature and technology. *Appl Mech Rev*. 72(5):050802.
13 Evans AR, *et al.* 2021. A universal power law for modelling the growth and form of teeth, claws, horns, thorns, beaks, and shells. *BMC Biol*. 19:58.
14 Broomell CC, *et al.* 2007. Mineral minimization in nature's alternative teeth. *J R Soc Interface*. 4(12):19–31.
15 Politi Y, Bertinetti L, Fratzl P, Barth FG. 2021. The spider cuticle: a remarkable material toolbox for functional diversity. *Philos Trans R Soc A*. 379(2206):20200332.
16 Mylo MD, Speck O. 2023. Longevity of system functions in biology and biomimetics: a matter of robustness and resilience. *Biomimetics*. 8(2):173.
17 Vincent JF. 1990. Fracture properties of plants. *Advances in botanical research (vol. 17)*. Academic Press. p. 235–287
18 Launey ME, Ritchie RO. 2009. On the fracture toughness of advanced materials. *Adv Mat*. 21(20):2103–2110.
19 Broeckhoven C, du Plessis A. 2017. Has snake fang evolution lost its bite? New insights from a structural mechanics viewpoint. *Biol Lett*. 13(8):20170293.
20 van der Meijden A, Kleinteich T. 2017. A biomechanical view on stinger diversity in scorpions. *J Anat*. 230(4):497–509.
21 Marom Z, Shtein I, Bar-On B. 2017. Stomatal opening: the role of cell-wall mechanical anisotropy and its analytical relations to the bio-composite characteristics. *Front Plant Sci*. 8:2061.
22 Du Plessis A, Broeckhoven C, Le Roux SG. 2018. Snake fangs: 3D morphological and mechanical analysis by microCT, simulation, and physical compression testing. *Gigascience*. 7(1):gix126.
23 Gershon S, Bar-On B, Sonnenreich S, Ayali A, Pinchasik BE. 2024. Asymmetry between the dorsal and ventral digging valves of the female locust: function and mechanics. *BMC Biol*. 22(1):129.
24 Lucas PW, Turner IM, Dominy NJ, Yamashita N. 2000. Mechanical defences to herbivory. *Ann Bot*. 86(5):913–920.
25 Gibson LJ. 2012. The hierarchical structure and mechanics of plant materials. *J R Soc Interface*. 9(76):2749–2766.
26 Oliver WC, Pharr GM. 1992. An improved technique for determining hardness and elastic modulus using load and displacement sensing indentation experiments. *J Mater Res*. 7(6):1564–1583.
27 De Magistris F, Salmén L. 2008. Finite element modelling of wood cell deformation transverse to the fibre axis. *Nord Pulp Paper Res J*. 23(2):240–246.
28 Niemz P, Sonderegger W, Gorbacheva G. 2023. Elastic and inelastic properties of wood and wood-based materials. *Springer handbook of wood science and technology*. Cham: Springer International Publishing. p. 399–439.
29 Bhushan B. 2013. *Principles and applications of tribology*. John wiley & sons.
30 Gindl W, Gupta HS, Schöberl T, Lichtenegger HC, Fratzl P. 2004. Mechanical properties of spruce wood cell walls by nanoindentation. *Appl Phys A*. 79:2069–2073.
31 Tze WTY, Wang S, Rials TG, Pharr GM, Kelley SS. 2007. Nanoindentation of wood cell walls: continuous stiffness and hardness measurements. *Compos Part A Appl Sci Manuf*. 38(3):945–953.
32 Konnerth J, Gierlinger N, Keckes J, Gindl W. 2009. Actual versus apparent within cell wall variability of nanoindentation results from wood cell walls related to cellulose microfibril angle. *J Mater Sci*. 44:4399–4406.

33 Burgert I, Keplinger T. 2013. Plant micro-and nanomechanics: experimental techniques for plant cell-wall analysis. *J Exp Bot*. 64(15):4635–4649.
34 Nicolás-Bermúdez J, *et al*. 2022. Characterization of the hierarchical architecture and micromechanical properties of walnut shell (*Juglans regia* L.). *J Mech Behav Biomed Mater*. 130:105190.
35 Leroux O, *et al*. 2018. Comparative in situ analysis reveals the dynamic nature of sclerenchyma cell walls of the fern *Asplenium rutifolium*. *Ann Bot*. 121(2):345–358.
36 Ezra Z, Levavi L, Bar-On B. 2023. The load-bearing mechanism of plant wings: a multiscale structural and mechanical analysis of the *T. tipu* samara. *Acta Biomater*. 158:423–434.
37 Amini S, Miserez A. 2013. Wear and abrasion resistance selection maps of biological materials. *Acta Biomater*. 9(8):7895–7907.
38 Zok FW, Miserez A. 2007. Property maps for abrasion resistance of materials. *Acta Mater*. 55(18):6365–6371.
39 Gorb EV, Popov V, Gorb S. 2002. Natural hook-and-loop fasteners: anatomy, mechanical properties, and attachment force of the jointed hooks of the Galium aparine fruit. *Des Nat*. 3:151–160.
40 Bauer G, *et al*. 2010. Always on the bright side: the climbing mechanism of Galium aparine. *Proc Roy Soc B*. 278(1715):2233–2239.
41 Huang F, Guo W. 2013. Structural and mechanical properties of the spines from *Echinocactus grusonii* cactus. *J Mater Sci*. 48: 5420–5428.
42 Bührig-Polaczek A, *et al*. 2016. Biomimetic cellular metals—using hierarchical structuring for energy absorption. *Bioinspir Biomim*. 11(4):045002.
43 Wang L, *et al*. 2023. Fracture resistance biomechanisms of walnut shell with high-strength and toughening. *Adv Sci*. 10(27):2303238.
44 Das S, Ghatak A. 2011. Puncturing of soft gels with multi-tip needles. *J Mater Sci*. 46:2895–2904.
45 Fakhouri S, Hutchens SB, Crosby AJ. 2015. Puncture mechanics of soft solids. *Soft matter*. 11(23):4723–4730.
46 Fregonese S, Bacca M. 2021. Piercing soft solids: a mechanical theory for needle insertion. *J Mech Phys Solids*. 154:104497.
47 Muthukumar M, Bobji MS, Simha KRY. 2022. Cone cracks in tissue-mimicking hydrogels during hypodermic needle insertion: the role of water content. *Soft Matter*. 18(18):3521–3530.
48 Zhang B, Anderson PS. 2022. Modelling biological puncture: a mathematical framework for determining the energetics and scaling. *J R Soc Interface*. 19(195):20220559.
49 Bar-On B, Barth FG, Fratzl P, Politi Y. 2014. Multiscale structural gradients enhance the biomechanical functionality of the spider fang. *Nat Commun*. 5(1):3894.
50 Schofield RMS, Nesson MH, Richardson KA, Wyeth P. 2003. Zinc is incorporated into cuticular "tools" after ecdysis: the time course of the zinc distribution in "tools" and whole bodies of an ant and a scorpion. *J Insect Physiol*. 49(1):31–44.
51 Lichtenegger HC, *et al*. 2003. Zinc and mechanical prowess in the jaws of Nereis, a marine worm. *Proc Natl Acad Sci U S A*. 100(16): 9144–9149.
52 Cribb BW, *et al*. 2008. Insect mandibles—comparative mechanical properties and links with metal incorporation. *Naturwissenschaften*. 95:17–23.
53 Politi Y, *et al*. 2012. A spider's fang: how to design an injection needle using chitin-based composite material. *Adv Funct Mater*. 22(12):2519–2528.
54 Kellersztein I, Cohen SR, Bar-On B, Wagner HD. 2019. The exoskeleton of scorpions' pincers: structure and micro-mechanical properties. *Acta Biomater*. 94:565–573.
55 Tadayon M, *et al*. 2020. Adaptations for wear resistance and damage resilience: micromechanics of spider cuticular "tools". *Adv Funct Mater*. 30(32):2000400.
56 Anderson PS. 2018. Making a point: shared mechanics underlying the diversity of biological puncture. *J Exp Biol*. 221(22):jeb187294.
57 Jensen KH, Knoblauch J, Christensen AH, Haaning KS, Park K. 2020. Universal elastic mechanism for stinger design. *Nat Phys*. 16(10):1074–1078.
58 Quan H, *et al*. 2024. The shape of Nature's stingers revealed. *Proc Natl Acad Sci U S A*. 121(7):e2316320121.
59 Bar-On B. 2019. On the form and bio-mechanics of venom-injection elements. *Acta Biomater*. 85:263–271.
60 Su FY, *et al*. 2017. Spines of the porcupine fish: structure, composition, and mechanical properties. *J Mech Behav Biomed Mater*. 73: 38–49.
61 Das R, *et al*. 2018. Biomechanical evaluation of wasp and honeybee stingers. *Sci Rep*. 8(1):14945.
62 Segall M, *et al*. 2023. Armed to the teeth: the underestimated diversity in tooth shape in snakes and its relation to feeding behavior and diet. *Ecol Evol*. 13(4):e10011.
63 Salerno G, *et al*. 2023. Coleoptera claws and trichome interlocking. *J Comp Physiol A*. 209(2):299–312.
64 Birkenfeld V, Gorb SN, Krings W. 2024. Mandible elemental composition and mechanical properties from distinct castes of the leafcutter ant *Atta laevigata* (Attini; Formicidae). *Interface Focus*. 14(2):20230048.
65 Hackethal S, Schulz-Kornas E, Gorb SN, Krings W. 2024. Wear patterns of radular teeth in *Loligo vulgaris* (Cephalopoda; Mollusca) are related to their structure and mechanical properties. *Interface Focus*. 14(2):20230082.
66 Gorb E, Gorb S. 2002. Contact separation force of the fruit burrs in four plant species adapted to dispersal by mechanical interlocking. *Plant Physiol Biochem*. 40(4):373–381.
67 Halpin JC. 2017. *Primer on composite materials analysis (revised)*. Routledge.
68 Bar-On B. 2023. The effect of structural curvature on the load-bearing characteristics of biomechanical elements. *J Mech Behav Biomed Mater*. 138:105569.
69 Zhang B, Baskota B, Chabain JJ, Anderson PS. 2024. Curving expectations: the minimal impact of structural curvature in biological puncture mechanics. *Sci Adv*. 10(33):eadp8157.
70 Soffiatti P, Rowe NP. 2020. Mechanical innovations of a climbing cactus: functional insights for a new generation of growing robots. *Front Robot AI*. 7:64.
71 Fiorello I, *et al*. 2020. Climbing plant-inspired micropatterned devices for reversible attachment. *Adv Funct Mater*. 30(38):2003380.
72 Speck O, Speck T. 2021. Functional morphology of plants–a key to biomimetic applications. *New Phytol*. 231(3):950–956.
73 Ohlendorf R, Tan NYH, Nakayama N. 2023. Engineering themes in plant forms and functions. *Annu Rev Plant Biol*. 74:777–801.